A Reduced Mass-Spring-Mass Model of Compliant Robots Dedicated to the Evaluation of Impact Forces

Guillaume Jeanneau, Vincent Bégoc, Sébastien Briot

A Reduced Mass-Spring-Mass Model of Compliant Robots Dedicated to the Evaluation of Impact Forces

Guillaume Jeanneau[a,b,d] **Vincent Bégoc**[a,c,*] **Sébastien Briot**[a,d]

[a] Laboratoire des Sciences du Numérique de Nantes (LS2N)
UMR CNRS 6004, 44321 Nantes, France
[b] École Centrale de Nantes (ECN)
[c] Institut Catholique d'Arts et Métiers (ICAM)
[d] Centre National de la Recherche Scientifique (CNRS)
Emails: {Guillaume.Jeanneau,Sebastien.Briot}@ls2n.fr, Vincent.Begoc@icam.fr

The introduction of intrinsic compliance in the design of robots allows to reduce the risk for humans working in the vicinity of a robotic cell. Indeed, it permits to decouple the dynamic effects of the links' inertia from those of the rotors' inertia, thus reducing the maximum impact force in case of a collision. However, robot designers are lacking modeling tools to help simulate numerous collision scenarios, analyze the behaviour of a compliant robot and optimize its design.

In this article, we introduce a method to reduce the dynamic model of a multi-link compliant robot to a simple translational mass-spring-mass system. Simulation results show that this reduced model allows to accurately predict the maximal impact force in case of a collision with a constrained human body part. Multiple impact scenarios are conducted on two case-studies, a planar serial elastic robot and the R-Min robot, an underactuated parallel planar robot, designed for collaboration.

1 INTRODUCTION

Recent years have shown a continuously growing interest in collaborative robotic applications, in which a robot and a human share a common workspace. This enables the robot to assist the human but, at the same time, generates hazardous situations of unexpected contact. A major concern in the design of such a collaborative robotic cell thus lies in the reduction of the human-related hazard under an acceptable level. The severity of injuries was originally investigated in the context of car-accidents for the automotive industry and led to criteria such as the HIC (Head Injury Criteria [1]). However, this criteria was shown to be unsuitable to evaluate the safety of a robotic cell [2, 3]. Since then, an international standard ISO/TS 15066 [4] was edited to guide designers through the risk assessment of a collaborative robotic workcell based on pressure and force pain thresholds evaluated for 29 body regions issued from an experimental study led on 100 subjects [5].

Based on these safety criteria, researchers have deeply investigated the role of multiple parameters on the severity of an impact in order to propose new concepts allowing to obtain intrinsically safer robots. In two early studies, the velocity and the reflected robot's mass at the end-effector were shown to play a major role on the severity of an unconstrained impact [3] and especially in the case of a constrained impact [6] (when the impacted human body region is clamped between the robot and a wall or any other rigid and fixed part of the workspace). This led to the development of lightweight robots [7, 8] to obtain a better trade-off between safety and productivity.

Another widely explored strategy, consists in the development of intrinsically compliant robots based on the use of new actuation approaches [9] such as Series Elastic Actuator (SEA) with fixed [10, 11] or variable stiffness [9], or the Distributed Macro-Min (DM^2) approach [12]. These compliant mechanisms are intended

*Address all correspondence to this author.

to decouple the effects of the links' inertia from those of the rotors' inertia, i.e. decorrelate the kinetic energy of the impacted link from the rotor's inertia and thus reduce the reflected mass [13] perceived at the contact point allowing to mitigate the impact severity. As pointed out in [14], the joint stiffness can be advantageously reduced only to a certain extent. Indeed, once the rotor's and the link's inertia have been decoupled, further reducing the joint stiffness will not reduce the impact force. The role of joint stiffness in the hazard reduction of a constrained impact was further investigated in [15] and shown to reduce the maximal impact force, providing even better results when associated to a collision detection and reaction strategy.

However, in most of the works studying the influence of the design parameters of a compliant mechanism on safety, the robot is reduced to a single rotating link mechanism [9, 14–16], which does not give any insight on how the configuration of a multi-dof compliant robot, the direction of impact, or the location of the impact on the robot's arm affects the severity of an impact. In [17], authors simulate the collision of a serial multi-link robot and simplify the problem by linearizing the equations of motion of the robot at the time of impact and by modelling the human body as a simple spring-mass system. In [15], authors give a method to compute the parameters of an equivalent mass-spring-mass model of a compliant multi-link serial robot, projecting the links' inertia matrix, the rotors' inertia matrix and the joint stiffness matrix along the direction of impact. However, no simulation of this reduced model was conducted on a multi-link robot to evaluate the relevance of the proposed parameters. In [18], authors directly derive a closed-form sinusoidal equation of the maximum impact force from the equations of motion of a three-mass oscillatory system. The human is therefore approximated as a spring-mass system, the reflected mass at the contact level is computed at the end-effector using [13] and the mass on the rotor's side is considered infinite. This approach is further investigated in [19] to approximate the reflected mass of the robot or the maximal impact force directly, considering a non-infinite mass rotor inertia. However, authors in [19] and [18] consider a fully elastic linear contact to help solve the equation of motion (neglecting the absorbing effect of the skin), thus generating conservative results.

In this article, we introduce a new method to compute the parameters of a reduced mass-spring-mass model of a compliant robot. This model allows to obtain the maximum impact force, in a computationally efficient manner, from the simulation of an impact between this reduced system and a human body part, considering the non-linear properties of the human body in the computation of the contact force. The proposed robot's model is based on the projection of the equations of motion in two dynamically independent subspaces. This method applies indifferently to compliant robots with serial or parallel architectures, however, it does not apply to robots using flexible links [20], disengaging mechanisms [16] or preloaded mechanism with mechanical stops [21]. Two different robots are considered as well as different locations of impact on the robot, i.e. on the end-effector or on the elbow. To the best of the authors' knowledge, most of the previous works have investigated an impact at the end-effector but nowhere else on the robot's arm. Simulation results show that the reduced model allows to obtain the impact force with a very good precision, for the two robots and for all impact scenarios and, furthermore, highlight the role of the joint stiffness in decoupling the links' and rotors' inertia of a multi-link robot and its effect on the maximum impact force.

The paper is organised as follows. The reduced mass-spring mass model is introduced in section 2. In section 3, simulation results of a constrained impact between a multi-link robot and a human body are conducted using the reduced model and compared with a full robot model. Two robots are considered: a two-link serial elastic robot and the R-Min robot, a planar compliant parallel robot. Multiple impact scenarios are investigated considering an impact at the end-effector or at the elbow, with the head or with the chest. A conclusion is drawn in section 4.

2 CALCULATION OF A REDUCED MASS-SPRING-MASS MODEL OF A ROBOT

2.1 Statement of the problem: definition of the target model

It has been shown for a single-link mechanism that the dynamic behaviour of a compliant mechanism can be reduced to an equivalent translational mass-spring-mass system [9, 15], consisting of a mass m_c perceived at the contact point, a mass m_a reflecting the inertia on the actuator side and, in between, the reflected stiffness of the robot k_r (see Fig. 1a).

The dynamics of a mass-spring-mass system is governed by the following equations:

$$\begin{bmatrix} m_c & 0 \\ 0 & m_a \end{bmatrix} \begin{bmatrix} \ddot{x}_c \\ \ddot{x}_a \end{bmatrix} + \begin{bmatrix} k_r & -k_r \\ -k_r & k_r \end{bmatrix} \begin{bmatrix} \Delta x_c \\ \Delta x_a \end{bmatrix} = \begin{bmatrix} f_c \\ 0 \end{bmatrix} \quad (1)$$

where x_c is the position of the reflected mass at the contact point m_c and x_a is the position of the reflected mass on the actuator's side m_a, and Δx_c, Δx_a their respective

displacements with respect to the spring unloaded position. f_c is the amplitude of the contact force, at the contact point, between the robot and, in the present article, the human body.

In what follows, we present a method to reduce the full dynamics model of a (multi-link) robot impacting its external environment (Fig. 1b) to the set of equations (1). This method is composed of the following steps:

1. First, the robot dynamics model is linearized around an equilibrium configuration (Sec. 2.2), considering that the impact is occurring during a very short interval of time,
2. Then, a new set of generalized coordinates is introduced (Sec. 2.3), composed of two types of coordinates: a coordinate at the impact point and coordinates written in a space orthogonal to the previous one, but dynamically consistent [13]. Projecting the linearized dynamics model on the space defined by this new set of coordinates allows the decoupling of the inertial effects occurring at the time of the impact.
3. Finally (Sec. 2.4), these new equations of motion are used to provide the expressions of the parameters m_c, k_r and m_a making the target model (1) as close as possible to the robot dynamics model during the impact.

Since we consider a multi-link robot, the parameters m_c, k_r and m_a of this reduced model depend on the location of the contact along the robot's arm (not necessarily at the end-effector), on the direction of impact, as well as on the configuration of the robot at the time of impact.

2.2 Linearization of the robot dynamics model

Let us consider a robot with n degrees-of-freedom and m motors ($n > m$). [1] We denote as $\mathbf{q}_g \in \mathbb{R}^n$ the set of generalized coordinates of the robots: the m first components of $\mathbf{q}_g$ correspond to the motor coordinates, and the $n - m$ remaining ones to the (uncontrolled) underactuated coordinates. The equation of motion of the robot is thus given by [22]:

$$\mathbf{M}(\mathbf{q}_g)\ddot{\mathbf{q}}_g + \mathbf{g}(\mathbf{q}_g) + \mathbf{c}(\mathbf{q}_g, \dot{\mathbf{q}}_g) = \mathbf{u} + \mathbf{f}_{ext} \qquad (2)$$

where $\mathbf{M}(\mathbf{q}_g)$ is the robot generalized inertia matrix, $\mathbf{g}(\mathbf{q}_g)$ is the vector regrouping the effect of conservative forces (e.g. gravity, deformations), $\mathbf{c}(\mathbf{q}_g, \dot{\mathbf{q}}_g)$ is the vector of Coriolis and centrifugal effects, $\mathbf{u} = [\boldsymbol{\tau}^T \ \mathbf{0}]^T$, with

[1] In what follows, we assume that all robots under consideration are underactuated, due to the introduction of compliance in the mechanical architecture and/or in the controller.

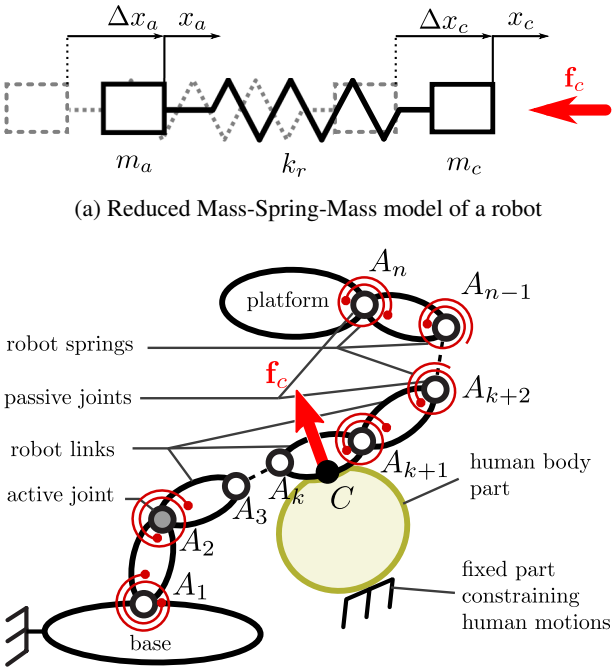

(a) Reduced Mass-Spring-Mass model of a robot

(b) A robot impacting with an external object such as a human body region.

Fig. 1: (a) A reduced Mass-Spring-Mass model of a robot and (b) a model of a compliant robot colliding with a human body.

$\boldsymbol{\tau} \in \mathbb{R}^m$ the vector of the motor input efforts. Finally, $\mathbf{f}_{ext}$ is the vector of the generalized external forces (in our case, the impact force).

The equation of motion (2) is linearized around an equilibrium configuration ($\mathbf{q}_g = \mathbf{q}_{g0}, \dot{\mathbf{q}}_g = \mathbf{0}, \ddot{\mathbf{q}}_g = \mathbf{0}$) (more details are given in Appendix A):

$$\mathbf{M}_0\ddot{\mathbf{q}}_g + \mathbf{K}_0\Delta\mathbf{q}_g = \Delta\mathbf{u} + \mathbf{f}_{ext} \qquad (3)$$

where $\Delta\mathbf{q}_g = \mathbf{q}_g - \mathbf{q}_{g0}$ is a variation of the generalized coordinates, $\Delta\mathbf{u} = \mathbf{u} - \mathbf{g}_0$ is a variation of the generalized input forces around the equilibrium and $\mathbf{f}_{ext}$ is the generalized contact force, $\mathbf{M}_0$ is the robot's inertia matrix computed at $\mathbf{q}_{g0}$ and $\mathbf{K}_0$ is the stiffness matrix of the robot (see App. A).

Let us consider the robot impacting an external object at a point C with coordinates $\mathbf{p}_c$, (Fig. 1b). The displacement of the contact point C along the normal vector $\mathbf{n}$ is denoted $\Delta x_c = \mathbf{n}^T\Delta\mathbf{p}_c$, with $\Delta\mathbf{p}_c$ the displacement of point C. Taking the hypotheses from the norm [4], we assume that the contact force $\mathbf{f}_c$ at C is directed along $\mathbf{n}$, i.e. $\mathbf{f}_c = f_c\mathbf{n}$ (no friction is considered at the contact).

We thus obtain the vector of the generalized impact force $\mathbf{f}_{ext} = \mathbf{J}_c^T f_c$ where matrix $\mathbf{J}_c \in \mathbb{R}^{1\times n}$ relates $\dot{x}_c$ to $\dot{\mathbf{q}}_g$ as:

$$\dot{x}_c = \mathbf{J}_c \dot{\mathbf{q}}_g \tag{4}$$

Since the impact peak force that we want to compute, only lasts a few milliseconds and assuming that the controller bandwidth is not high enough to react to this high-frequency phenomenon, the variation $\Delta\mathbf{u}$ is assumed to be null in the vicinity of the impact time. We finally obtain the linearized approximation of Eq. (3):

$$\mathbf{M}_0 \ddot{\mathbf{q}}_g + \mathbf{K}_0 \Delta\mathbf{q}_g = \mathbf{J}_c^T f_c \tag{5}$$

In the next section, a new set of generalized coordinates is defined allowing to decouple the inertial effects of Eq. (5).

2.3 Definition of a new set of generalized coordinates

Similarly as what is done when projecting the robot dynamics in the task space [23], we project the linearized dynamics model (5) in a space defined by a new set of generalized coordinates containing x_c, i.e. the generalized coordinate of the impact point, and some other coordinates lying in a space orthogonal to x_c, but dynamically consistent [13]. As shown later below, projecting the linearized dynamics model on a space defined by this new set of coordinates, allows to decouple the inertia perceived at the impact location from the remaining inertia on the actuator's side.

Let us define as $\mathbf{q}_n = [x_c \ \mathbf{x}_a^T]^T \in \mathbb{R}^n$ this new set of generalized coordinates, containing the variable x_c and a vector $\mathbf{x}_a \in \mathbb{R}^{n-1}$ which is further defined. The set of coordinates $\mathbf{x}_a$ reflects internal motions of the robot whose inertia does not directly affect the acceleration of the contact point. The generalized velocity $\dot{\mathbf{q}}_g$ can be expressed as a function of $\dot{\mathbf{q}}_n$ through the following generic relationship:

$$\dot{\mathbf{q}}_g = \mathbf{E}_c \dot{x}_c + \mathbf{E}_a \dot{\mathbf{x}}_a \tag{6}$$

where $\mathbf{E}_c \in \mathbb{R}^{n\times 1}$ and $\mathbf{E}_a \in \mathbb{R}^{n\times(n-1)}$ are two matrices whose expressions will be provided below.

Left-multiplying Eq. (6) by $\mathbf{J}_c$, we obtain:

$$\dot{x}_c = \mathbf{J}_c\mathbf{E}_c \dot{x}_c + \mathbf{J}_c\mathbf{E}_a \dot{\mathbf{x}}_a \tag{7}$$

Equations (4) and (7) imply the following properties for matrices $\mathbf{E}_c$ and $\mathbf{E}_a$ to be satisfied:

$$\mathbf{J}_c\mathbf{E}_c = 1, \ \mathbf{J}_c\mathbf{E}_a = \mathbf{0} \tag{8}$$

This means that $\mathbf{E}_c$ is a right-hand-side generalized inverse of $\mathbf{J}_c$. In the following, we use a dynamically consistent generalized inverse $\mathbf{J}_c^{\#} \in \mathbb{R}^{n\times 1}$ of $\mathbf{J}_c$ as defined in [13]:

$$\mathbf{J}_c^{\#} = \mathbf{M}_0^{-1}\mathbf{J}_c^T m_c = \mathbf{E}_c \tag{9}$$

where m_c is the reflected mass of the robot at the contact point C computed as follows:

$$m_c = \left(\mathbf{J}_c\mathbf{M}_0^{-1}\mathbf{J}_c^T\right)^{-1} \tag{10}$$

Now, let us focus on the definition of matrix $\mathbf{E}_a$. The time-derivative of any set of robot coordinates $\mathbf{x}_a$ could be defined thanks to the generalized velocities $\dot{\mathbf{q}}_g$ by a generic relation:

$$\dot{\mathbf{x}}_a = \mathbf{J}_a \dot{\mathbf{q}}_g \tag{11}$$

where $\mathbf{J}_a \in \mathbb{R}^{(n-1)\times n}$ is the Jacobian matrix relating $\dot{\mathbf{x}}_a$ to $\dot{\mathbf{q}}_g$. Left-multiplying Eq. (6) by $\mathbf{J}_a$, we get:

$$\dot{\mathbf{x}}_a = \mathbf{J}_a\mathbf{J}_c^{\#}\dot{x}_c + \mathbf{J}_a\mathbf{E}_a\dot{\mathbf{x}}_a \tag{12}$$

Equations (11) and (12) imply the following properties for matrices $\mathbf{E}_a$ and $\mathbf{J}_a$ to be satisfied:

$$\mathbf{J}_a\mathbf{E}_a = \mathbf{I}_{(n-1)\times(n-1)}, \ \mathbf{J}_a\mathbf{J}_c^{\#} = \mathbf{0} \tag{13}$$

where $\mathbf{I}_{(n-1)\times(n-1)}$ is the identity matrix of dimension $n-1$. The left-hand side of (13) means that $\mathbf{E}_a$ is a right-hand-side generalized inverse $\mathbf{J}_a^{\#} \in \mathbb{R}^{n\times(n-1)}$ of $\mathbf{J}_a$: $\mathbf{E}_a = \mathbf{J}_a^{\#}$. We also see from the right-hand side of (13) that, indeed, $\mathbf{J}_a^T$ spans the nullspace of $\mathbf{J}_c^{\#T}$. Then, from (9), the transpose of $\mathbf{J}_a$ can be computed as:

$$\mathbf{J}_a^T = \ker(\mathbf{J}_c^{\#T}) = \ker(\mathbf{J}_c\mathbf{M}_0^{-1}) \tag{14}$$

It should be mentioned that, by definition, matrix $\mathbf{M}_0$ is symmetric positive definite [22].

As proven in Appendix B, matrix $\mathbf{J}_a^{\#}$ is given by:

$$\mathbf{J}_a^{\#} = \mathbf{M}_0^{-1}\mathbf{J}_a^T\mathbf{M}_a = \mathbf{E}_a \tag{15}$$

where $\mathbf{M}_a \in \mathbb{R}^{(n-1)\times(n-1)}$ is the pseudo-kinetic energy matrix associated to the coordinates $\mathbf{x}_a$ defined by Khatib in [13]:

$$\mathbf{M}_a = (\mathbf{J}_a\mathbf{M}_0^{-1}\mathbf{J}_a^T)^{-1} \tag{16}$$

The dynamic decoupling of these two inertia appears when projecting the linearized dynamic model expressed in the joint space (5) in the contact space by $\mathbf{J}_c^{\#T}$ and, in a complementary space, by $\mathbf{J}_a^{\#T}$:

$$\mathbf{J}_c^{\#T}(\mathbf{M}_0\ddot{\mathbf{q}}_g + \mathbf{K}_0\Delta\mathbf{q}_g) = \mathbf{J}_c^{\#T}\mathbf{J}_c^T f_c \tag{17}$$
$$\mathbf{J}_a^{\#T}(\mathbf{M}_0\ddot{\mathbf{q}}_g + \mathbf{K}_0\Delta\mathbf{q}_g) = \mathbf{J}_a^{\#T}\mathbf{J}_c^T f_c \tag{18}$$

Using Eq. (9), Eq. (15) and the symmetry of $\mathbf{M}_0$, the two equations above become:

$$m_c\mathbf{J}_c\ddot{\mathbf{q}}_g + \mathbf{J}_c^{\#T}\mathbf{K}_0\Delta\mathbf{q}_g = f_c \tag{19}$$
$$\mathbf{M}_a\mathbf{J}_a\ddot{\mathbf{q}}_g + \mathbf{J}_a^{\#T}\mathbf{K}_0\Delta\mathbf{q}_g = \mathbf{0} \tag{20}$$

Since the model is linearised around an equilibrium configuration for which $\dot{\mathbf{q}}_g \approx 0$ (see Eq. (40) in App. A), the time-derivative of Eq. (4) and (11) gives:

$$\ddot{x}_c \approx \mathbf{J}_c\ddot{\mathbf{q}}_g,\ \ddot{\mathbf{x}}_a \approx \mathbf{J}_a\ddot{\mathbf{q}}_g \tag{21}$$

Using Eqs. (6), (9) and (15) and assuming small displacements, we may write:

$$\Delta\mathbf{q}_g = \mathbf{J}_c^{\#}\Delta x_c + \mathbf{J}_a^{\#}\Delta\mathbf{x}_a \tag{22}$$

Then, using Eqs. (21) and (22), the system of Eqs. (19) and (20) becomes:

$$m_c\ddot{x}_c + \mathbf{J}_c^{\#T}\mathbf{K}_0\mathbf{J}_c^{\#}\Delta x_c + \mathbf{J}_c^{\#T}\mathbf{K}_0\mathbf{J}_a^{\#}\Delta\mathbf{x}_a = f_c \tag{23}$$
$$\mathbf{M}_a\ddot{\mathbf{x}}_a + \mathbf{J}_a^{\#T}\mathbf{K}_0\mathbf{J}_c^{\#}\Delta x_c + \mathbf{J}_a^{\#T}\mathbf{K}_0\mathbf{J}_a^{\#}\Delta\mathbf{x}_a = \mathbf{0} \tag{24}$$

This set of equations permits to show that there exists a set of generalized coordinates $\mathbf{q}_n = [x_c\ \mathbf{x}_a^T]^T$ allowing to describe the dynamics of the robot with two equations of motion using independent inertia m_c and $\mathbf{M}_a$. Indeed, when considering a null joint stiffness $\mathbf{K}_0 = \mathbf{0}$, the acceleration of x_c would not affect the acceleration of $\mathbf{x}_a$ and reversely, i.e. the inertial effects would be decoupled. The set of coordinates $\mathbf{x}_a$, which is defined here as a set of coordinates orthogonal to x_c, is thus said to evolve in a *dynamically complementary space* with respect to the coordinate x_c.

2.4 Computing the parameters of the reduced model

Let us introduce the reflected stiffness of the robot at the contact level:

$$k_r = \mathbf{J}_c^{\#T}\mathbf{K}_0\mathbf{J}_c^{\#} \tag{25}$$

which allows to rewrite (23) as:

$$m_c\ddot{x}_c + k_r\Delta x_c + \mathbf{J}_c^{\#T}\mathbf{K}_0\mathbf{J}_a^{\#}\Delta\mathbf{x}_a = f_c \tag{26}$$

The vector $\Delta\mathbf{x}_a$ is projected onto a one-dimensional space to obtain a scalar displacement Δx_a, such that $\Delta x_a = \mathbf{J}_x\Delta\mathbf{x}_a$, with $\mathbf{J}_x$ a Jacobian matrix defined by:

$$-k_r\mathbf{J}_x = \mathbf{J}_c^{\#T}\mathbf{K}_0\mathbf{J}_a^{\#} \tag{27}$$

thus leading to:

$$m_c\ddot{x}_c + k_r\Delta x_c - k_r\Delta x_a = f_c \tag{28}$$

which is nothing else than the first line of Eq. (1).

Now, left-multiplying the second line of (1) by $\mathbf{J}_x^T$ and considering $\ddot{x}_a \approx \mathbf{J}_x\ddot{\mathbf{x}}_a$ around the equilibrium point, we get:

$$m_a\mathbf{J}_x^T\mathbf{J}_x\ddot{\mathbf{x}}_a - k_r\mathbf{J}_x^T\Delta x_c + k_r\mathbf{J}_x^T\mathbf{J}_x\Delta x_a = \mathbf{0} \tag{29}$$

Equations (24) and (29) are equivalent if and only if:

$$m_a\mathbf{J}_x^T\mathbf{J}_x = \mathbf{M}_a \tag{30}$$
$$-k_r\mathbf{J}_x^T = \mathbf{J}_a^{\#T}\mathbf{K}_0\mathbf{J}_c^{\#} \tag{31}$$
$$k_r\mathbf{J}_x^T\mathbf{J}_x = \mathbf{J}_a^{\#T}\mathbf{K}_0\mathbf{J}_a^{\#} \tag{32}$$

Equations (31) and (27) are equivalent, using the symmetry of $\mathbf{K}_0$. From Eq. (30), we obtain:

$$\mathbf{J}_x^T\mathbf{J}_x = \frac{1}{m_a}\mathbf{M}_a \tag{33}$$

and from Eq. (32):

$$\mathbf{J}_x^T \mathbf{J}_x = \frac{1}{k_r} \mathbf{J}_a^{\#T} \mathbf{K}_0 \mathbf{J}_a^{\#} \tag{34}$$

For Eqs. (24) and (29) to be equal and for the robot to be equivalent to the target translational mass-spring-mass system, the following expression must be satisfied:

$$\frac{1}{m_a} \mathbf{M}_a - \frac{1}{k_r} \mathbf{J}_a^{\#T} \mathbf{K}_0 \mathbf{J}_a^{\#} = \mathbf{0} \tag{35}$$

Since this expression cannot be true in general, we now compute the mass m_a, corresponding to the reflected mass on the actuator's side introduced in Eq. (1), which makes the left-hand side of Eq. (35) as close as possible to zero (minimizing the matrix norm). Therefore, summarizing the results of this section, the parameters of the reduced mass-spring-mass model defined by Eq. (1) can be computed using the following expressions:

$$m_c = \left(\mathbf{J}_c \mathbf{M}_0^{-1} \mathbf{J}_c^T\right)^{-1} \tag{36}$$

$$k_r = \mathbf{J}_c^{\#T} \mathbf{K}_0 \mathbf{J}_c^{\#} \tag{37}$$

$$m_a = \text{argmin} \left(\left\| k_r \mathbf{M}_a - m_a \mathbf{J}_a^{\#T} \mathbf{K}_0 \mathbf{J}_a^{\#} \right\| \right) \tag{38}$$

It should be noted that the proposed reflected stiffness k_r is different from the stiffness projected along the direction of impact given in [15, 24], which is equal to $k_c = \left(\mathbf{J}_c \mathbf{K}_0^{-1} \mathbf{J}_c^T\right)^{-1}$. The proposed reflected stiffness k_r relies on the use of the dynamically consistent generalized inverse $\mathbf{J}_c^{\#}$ [13] and thus depends on the robot's inertia matrix. As show in Appendix B of [25], the stiffness k_c has a physical meaning in the static case but not really in the dynamic case, when the effect of inertia on contact forces cannot be neglected.

In the next Section, we validate our simplified model on several simulated case studies.

3 CASE STUDIES

In this section, simulation results are presented in order to assess the validity of the reduced mass-spring-mass robot model for representing the dynamic behaviour of a robot during a collision with a human body part and especially determining the maximum impact force.

Two different planar robot architectures are considered including both open and closed-chain mechanisms. The first robot is a serial RR robot with parallel rotational joints actuated by Series Elastic Actuators (SEA). The second robot is the R-Min robot [26,27], a parallel seven-bar underactuated mechanism, designed for safe physical interactions with a human being.

For each robot, various impact scenarios are compared, considering different robot configurations and different contact locations (at the End-Effector (EE) or at the elbow). Most of the simulations consider an impact with the head, but results are also given considering an impact with the chest.

3.1 Simulation methodology

In what follows, more details are given on simulations conducted using the reduced mass-spring-mass robot model (Eq. (1)) on the one hand, and using the multi-body robot model (Eq. (2)) on the other hand. In both cases, a robot interacts with an external object, more specifically a human body region in the context of this article. The contact model is based on the Hertz theory and permits to consider the non-linear properties of the skin since it has a major positive effect on the resulting impact force [16]. Details are also given on the controller used in the simulation of the multi-body robot since it affects the stiffness properties and thus the impact force.

3.1.1 Modeling of the impacted body region

In the simulation of a multi-body robot impacting an external body, the contact force can have any direction in space. For simplification purpose, no friction is considered such that the contact force is aligned with the vector $\mathbf{n}$ normal to the surface of the impacted body region at the contact point. Figure 2 represents the considered model for the human body, oriented along the contact normal vector $\mathbf{n}$, where k_h represents the stiffness of the human body part ($k_h = 150.10^3$ N/m for the head and $k_h = 25.10^3$ N/m for the chest [2]). A small damping $c_h = 10$ N.m^{-1}s^{-1} and mass $m_0 = 0.00001$ kg have been introduced to avoid chattering in the simulation.

3.1.2 Contact modeling

The skin has a compliant behaviour which significantly reduces the peak impact force. In the simulations, the mechanical properties of the skin are derived from those of the damping material recommended in [28] for the design of a biofidelic measurement system for the safety assessment of collaborative robotic workcells. Indeed, the skin is replaced by a rubber foam with specified thickness and hardness aimed to mimic the biomechanical properties of the impacted body region. In the simu-

[2] The corresponding biomechanical properties have been specified according to the standards ISO/TS 15066 [4].

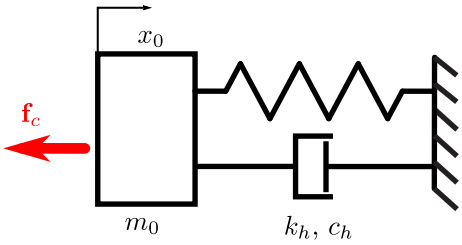

Fig. 2: Simplified model of an impacted human body region for a constrained collision, with x_0 the position of the impacted human body part along the contact normal $\mathbf{n}$.

lation results presented in the following, the contact force f_c is obtained using the Hertz contact theory, considering an elastic contact, with a power exponent $n_f = 1.5$ and a stiffness $k_f = 1.9{\cdot}10^7$ N.m$^{(-n_f)}$ obtained experimentally using a foam of 7 mm thickness and 70 ShA hardness (as recommended in [28] for mimicking the head and chest).

3.1.3 Discussion on control strategies

In the simulation of the full robot model, the actuator torques are computed using a computed torque control [22] applied in the active joint space, using the equations of motion given in (2). A PID controller is chosen to compensate errors in the model and to obtain a realistic behaviour. The derivative k_d, proportional k_p and integral k_i controller gains are chosen using the theory given in [22]. In the reduced model, the proportional gain of the controller is considered in the computation of the reflected stiffness.

In the simulation of the full robot model, a reactive strategy is implemented to reproduce an impact detection such that the motor torques compensate the forces derived from the potential energy, 20 ms after detecting the impact. In the simulation of the reduced model, no control nor reactive strategy is introduced, but an initial velocity v_0 is simply imposed to m_a and m_c, corresponding to the impact velocity obtained with the full robot model. Unless otherwise specified, this velocity is chosen as $v_0 = 1$ m/s.

3.2 Serial elastic RR robot

3.2.1 Robot description

The considered robot, in this section, is a serial RR robot actuated by two rotational SEA (Fig. 3), consisting of a motor with a gear train, a rigid link and a rotational spring in between. The mechanism is thus composed of four bodies (two rotating inertia and two rigid links) and two springs with a supposed identical stiffness k_s. The

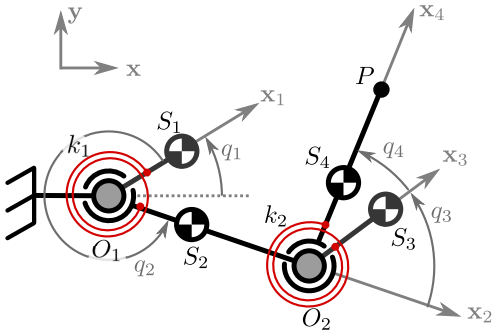

Fig. 3: Representation of the serial elastic RR robot. Coordinates q_1 and q_3 are actuated by two motors at O_1 and O_2, while coordinates q_2 and q_4 are passively driven by a rotational spring.

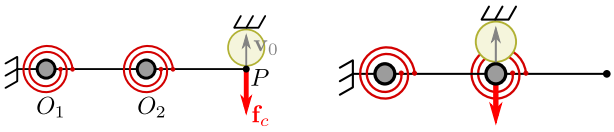

(a) impact on the end effector with an extended arm

(b) impact on the joint with an extended arm

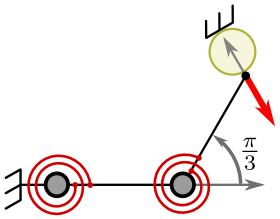

(c) impact on the end effector with a folded arm

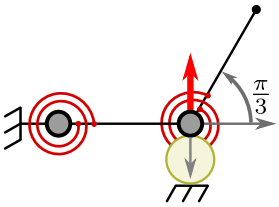

(d) impact on the joint with a folded arm

Fig. 4: Description of the four simulated scenarios for the serial elastic RR robot.

geometric and inertia properties of the four bodies are given in Table 1. The robot has four degrees of freedom and its configuration is parametrized by four angles $\mathbf{q} = [q_1, q_2, q_3, q_4]^T$, where q_1 (resp. q_3) is the angular position of the output shaft of motor M_1 (resp. M_2), and q_2 (resp. q_4) is the deflection angle of the spring k_1 (resp. k_2) from its unloaded position.

In the simulations of the full robot model presented below, the motor torques are computed using the PID controller presented in Part. 3.1.3 with the following parameters $k_d = 121$ rad/s, $k_p = 6050$ rad/s^2 and $k_i = 1.25 \cdot 10^5$ rad/s^3.

Table 1: Geometric and inertia properties of the elastic RR robot

Link	**Length**	**Mass**	**Inertia**[1]	**COM**[2]
i	l_i (m)	m_i (kg)	J_i (kg.m^2)	x_i (m)
1	0	1.5	4.71	0
2	0.5	17.4	0.539	0.068
3	0	1.5	0.83	0
4	0.5	6.04	0.086	0.143

[1] Moments of inertia around **z** are provided at the COM (Center Of Mass).
[2] COM S_2 (resp. S_4) (Fig. 3) are located on the lines O_1O_2 (resp. O_2P). x_i is the distance from O_1 (resp. O_2) to S_i for $i = \{1, 2\}$ (resp. $i = \{3, 4\}$).

3.2.2 *Considered impact scenarios*

In the following, multiple simulations are conducted considering four different impact scenarios depicted on Fig. 4:

a) the robot arm lies in a straight configuration (defined below) impacting at the EE (point P – Fig. 4a),
b) the robot arm lies in a straight configuration impacting at the elbow (point O_3– Fig. 4b),
c) the robot arm lies in a folded configuration (defined below) impacting at the EE (point P– Fig. 4c),
d) the robot arm lies in a folded configuration impacting at the elbow (point O_3– Fig. 4d).

The configuration of the robot at the time of impact is given by $\mathbf{q}^{(0)} = \mathbf{0}$ for cases (a) and (b), and $\mathbf{q}^{(0)} = [0, 0, \frac{\pi}{3}, 0]^T$ for cases (c) and (d). Indeed, robots are assumed to be in static equilibrium at the time of impact, rotational springs are thus unloaded since the gravity acceleration is directed along the **z** axis having no effect on the impact force.

The vector of joint velocities of the robot at the time of impact is imposed as $\dot{\mathbf{q}}^{(0)} = [\dot{q}_1^{(0)}, 0, 0, 0]^T$ for scenario (a-c) and $\dot{\mathbf{q}}^{(0)} = [-\dot{q}_1^{(0)}, 0, 0, 0]^T$ for scenario (d), where $\dot{q}_1^{(0)}$ is chosen as $\left\{ \frac{v_0}{\ell_2+\ell_4}, \frac{v_0}{\ell_2}, \frac{2/\sqrt{3}v_0}{\ell_2+\ell_4}, \frac{v_0}{\ell_2} \right\}$ for scenarios {a, b, c, d} respectively.

3.2.3 *Parameters of the mass-spring-mass model*

The parameters of the reduced mass-spring-mass robot model m_c, k_r and m_a are evaluated at the time of impact using equations (36), (25) and (38) respectively. The reflected mass at the contact location m_c depends on the robot's configuration, on the contact location and on the contact normal direction, but does not depend on the joint stiffness neither on the velocity. It has thus a constant value $m_c = \{0.73, 6.46, 1.12, 9.13\}$ kg for scenarios {a, b, c, d} respectively. It can be observed from these values that the reflected mass at the contact location m_c is lower when the impact occurs at the EE rather that at the elbow, and also when the arm is in a straight configuration rather than in a folded one.

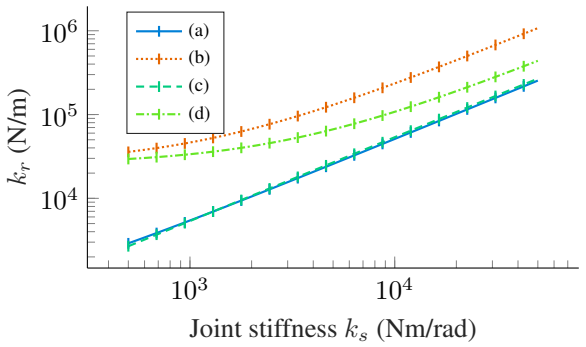

Fig. 5: Evolution of the reflected stiffness k_r with respect to the joint stiffness k_s for the four impact scenarios of the serial elastic RR robot.

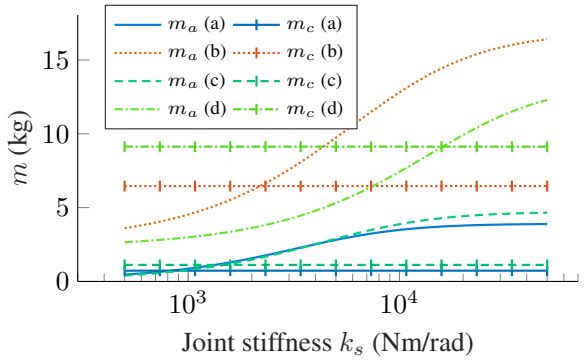

Fig. 6: Evolution of the reflected mass on the actuator side m_a with respect to the joint stiffness k_s for the four impact scenarios of the serial elastic RR robot.

Figure 5 shows that the reflected robot stiffness increases quasi-linearly with the joint stiffness k_s. Figure 6 shows that the reflected mass on the actuator side m_a significantly depends on the joint stiffness k_s and increases non-linearly with k_s.

3.2.4 Simulation analysis

In this paragraph, simulation results are presented for different values of the joint stiffness $k_s \in [5.10^2, 5.10^4]$ N.m/rad and different values of the impact velocity $v_0 \in [0.25, 2.5]$ m/s.

Varying the joint stiffness Figure 7 presents the impact force time profiles obtained from the simulation of the impact scenario (a) using the full robot model (solid blue curves) compared with those of the corresponding reduced mass-spring-mass model (dashed red curves). Simulations have been conducted for multiple values of the joint stiffness k_s and an impact velocity of 1 m/s. These results show that the simulation of the reduced model not only gives a good approximation of the maximum impact force, but also of the dynamic behaviour of the impact force during the first instants after the impact. It is thus possible to deduce the maximal stiffness allowing to dynamically decouple the inertia effects of the reflected mass at the contact m_c from that of the reflected mass on the actuator side m_a. Indeed, it can be observed from Fig. 7 that, for a joint stiffness $k_s \leq 4056$ N.m/rad, multiple isolated and short force peaks occur during the first instants after the impact with the head, whereas for higher joint stiffnesses, these isolated impacts progressively merge into a single higher and longer force peak, increasing the severity of the impact for the human.

Since this reduced model aims to approximate the severity of an impact, we further focus on the maximal impact force of the first impact. Indeed, once the impact has been detected, the second force peak could be mitigated using appropriate collision detection and reaction strategies [29], while the first contact is hardly avoidable. Figure 8 represents the maximal impact force of the first contact as a function of the joint stiffness k_s for the four scenarios, obtained simulating the full or the reduced model of the robot model. These results show that the reduced mass-spring-mass model can accurately predict the maximal impact force for the four scenarios considering an impact with the head with a mean absolute error of $\{1.8, 8.7, 1.9, 6.2\}$ % for scenarios {a, b, c, d} respectively (Fig. 8a). Similar results are obtained when considering an impact with the chest showing a mean error of respectively $\{2.8, 6.8, 2.8, 7.7\}$ % (Fig. 8b).

It can be observed, from Fig. 8, that the impact force is larger when the impact occurs at the elbow (scenarios (b,d)) rather than at the EE (scenarios (a,c)), for an identical impact velocity. This shows the interest of considering not only impacts at the end-effector but also on other parts of the robot's arm.

As a matter of comparison, simulations of a model considering a single reflected mass m_c instead of the proposed reduced mass-spring-mass system, provide a maximum impact force of $\{291, 903, 363, 1079\}$ N for an impact on the head resulting in an error of $\{11.0, 23.5, 9.6, 14.3\}$ % (for scenarios {a, b, c, d} respectively and considering an impact velocity of 1 m/s) and $\{152, 387, 156, 462\}$ N for an impact on the chest resulting in an error of $\{30.9, 32.1, 28.8, 21.8\}$ %. This model would systematically underestimate the impact force.

Varying the impact velocity Figure 9 compares the maximum impact force obtained from the simulation of the full model or the mass-spring-mass model, for the four impact scenarios, considering different values of the impact velocity and a constant joint stiffness of 10^5 N.m/rad. The parameters of the reduced model for scenarios {a, b, c, d} respectively are $m_a = \{3.49, 12.8, 3.88, 7.43\}$ kg, $k_r = \{5.1, 23.5, 5.4, 10.8\}$ 10^4 N/m. For both robot models, the impact force evolves linearly with the impact velocity. The reduced model permits to approximate the impact force with a maximal error of $\{0.55, 4.8, 0.3, 8.2\}$ % for scenarios {a, b, c, d} respectively.

Discussion In this paragraph, we showed that it is possible to represent the dynamic behaviour of a compliant serial robot during collision using the reduced mass-spring-mass system introduced in section 2. The simulation of such model allows to obtain a good approximation of the maximum impact force for different impact scenarios. This model also allows to identify the joint stiffness that decouples the inertia m_c and m_a, which depends on the configuration of the robot, on the location of the impact on the robot's arm and on the impacted body region. In what follows, we evaluate the relevance of the reduced model for an underactuated parallel robot.

3.3 R-Min robot: an underactuated parallel robot

In this section, we show that the reduced mass-spring-mass model also allows to accurately approximate the maximal impact force occurring during a collision between a compliant robot having a parallel architecture and a human body. We consider the R-Min [3] robot as a case-study, a robot designed for intrinsically safe collaboration with human [26, 27, 30].

[3] In this article, we consider a modified version of the R-Min robot presented in [30] where the preload system is replaced by two rotational springs located on the distal joints O_{i3}.

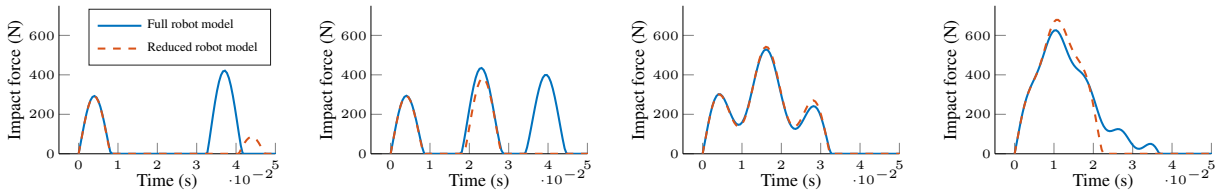

(a) $k_s = 500$ Nm/rad (b) $k_s = 1756$ Nm/rad (c) $k_s = 9369$ Nm/rad (d) $k_s = 50000$ Nm/rad

Fig. 7: Comparison of the contact force time profiles obtained from the simulation of the full robot model (solid blue curves) and the reduced mass-spring-mass robot model (dashed red curves), for different values of the joint stiffness k_s, in the scenario (a): the serial elastic RR robot impacting the head, at the EE, in a straight configuration, considering an impact velocity of 1 m/s.

Table 2: Dimensions and mass properties of the prototype links

Link	**Length**	**Mass**	**Inertia**[1]	**COM**[2]
$(i;j)$	$l_{i,j}$ (m)	$m_{i,j}$ (kg)	$J_{i,j}$ (kg.m^2)	$x_{i,j}$ (m)
(1&2;1)	0.28	6.92	0.033	0.015
(1&2;2)	0.2	0.26	0.0021	0.120
(1&2;3)	0.2	0.20	0.0016	0.100

[1] Moments of inertia around $\mathbf{z}$ are provided at the COM.
[2] Center of masses S_{ij} (Fig. 10) are located on the lines $O_{ij}O_{ij+1}$. $x_{i,j}$ is the distance from S_{ij} to O_{ij}.

3.3.1 *Presentation of the robot*

The R-Min robot (see Fig. 10) consists of a seven-bar mechanism, with five passive revolute joints on points O_{i2}, O_{i3} and at the EE P, and two active revolute joints on O_{i1} $(i = 1, 2)$ allowing to actuate the robot. All revolute joints have for axis $\mathbf{z}$ making this robot move in the vertical plane $\mathcal{P}_0 : (O_{11}, \mathbf{x}, \mathbf{z})$. This mechanism is underactuated since it has four dofs and two motors. Two rotational springs of stiffness k_s are added on the distal joints at points O_{13} and O_{23}, to increase the robot's stiffness and make it more easily controllable. These springs are considered to be unloaded when $q_{i3} = 0$.

The geometric and inertia properties used in the following simulations are issued from the CAD-model of the R-Min robot presented in [27] (see Tab. 2). The controlled torques are computed using the PID controller presented in Part. 3.1.3 with the following parameters $k_d = 51$ rad/s, $k_p = 1076$ rad/s^2 and $k_i = 9.26 \cdot 10^3$ rad/s^3.

3.3.2 *Considered impact scenarios*

In the following, multiple simulations are conducted considering two different impact scenarios with the R-Min robot depicted on Fig. 11:

e) the R-Min robot impacting at the EE (point P – Fig. 11a),
f) the R-Min robot impacting at the elbow (point O_{13} – Fig. 11b).

The configuration of the R-Min robot at the time of impact is arbitrarily defined by $\mathbf{q}_1^{(0)} = \begin{bmatrix} q_{11} & q_{21} \end{bmatrix}^T = \begin{bmatrix} -130.6^\circ & -50.0^\circ \end{bmatrix}^T$, the passive coordinates are computed so that the robot is in static equilibrium by solving the direct geometrico-static problem as formulated in [26]. Since the gravity is considered (pointing towards the $-\mathbf{z}$ direction), the joint springs are close to the unloaded position at equilibrium and the distal arms are slightly misaligned, allowing to compute the reflected stiffness k_r.

In both scenarios (e) and (f), the impact velocity $\mathbf{v}_0$ is chosen along the $\mathbf{x}$ direction with a norm of 1 m/s. The velocity of distal passive joints is assumed to be null $\dot{\mathbf{q}}_3^{(0)} = \mathbf{0}$. This results in the following actuators' velocity $\dot{\mathbf{q}}_1^{(0)} = \begin{bmatrix} -2.80 & -2.74 \end{bmatrix}^T$ (rad/s) in case (e) and $\dot{\mathbf{q}}_1^{(0)} = \begin{bmatrix} -2.80 & -5.00 \end{bmatrix}^T$ (rad/s) in case (f).

3.3.3 *Parameters of the mass-spring-mass model*

We obtain a reflected mass at the contact level of $m_c = \{1.17, 0.44\}$ kg for scenarios $\{\text{e}, \text{f}\}$ respectively. The evolution of the reflected mass on the actuator side m_a with the joints stiffness k_s is represented on Fig. 12. Likewise the serial elastic RR robot, the reflected stiffness k_r of the R-Min robot evolves quasi-linearly with respect to the joint stiffness k_s (Fig. 13).

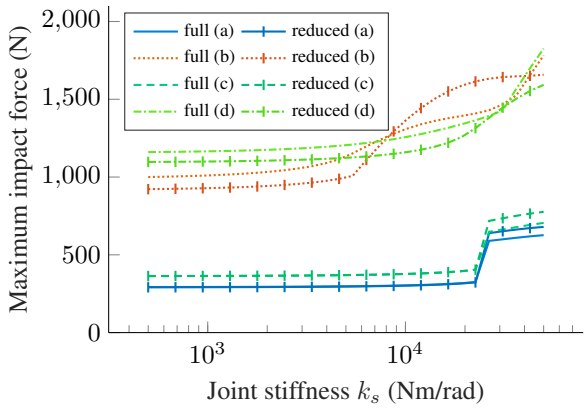

(a) Impact with the head

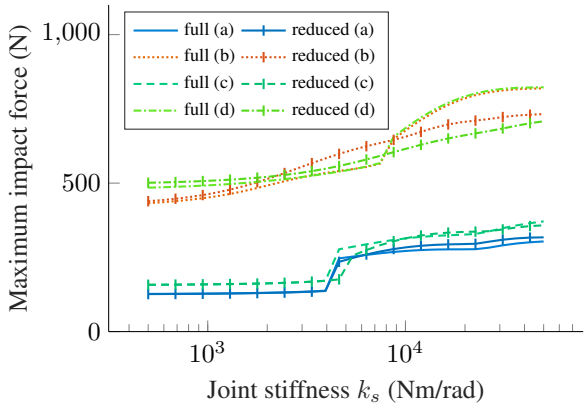

(b) Impact with the chest

Fig. 8: Comparison of the maximum impact force obtained by simulation using the full model or the reduced mass-spring-mass model of the serial elastic RR robot, for the four impact scenarios (a) with the head ($k_h = 150$ N/mm), (b) with the chest ($k_h = 25$ N/mm), considering an impact velocity of 1 m/s.

3.3.4 Simulation analysis

Varying the joint stiffness Figure 14 presents the impact force time profiles obtained from the simulation of the impact scenario (f): a collision between the R-Min robot at the elbow O_{13} and the head. These results show that the reduced model gives a good approximation of the dynamic behaviour of the impact force during the first instants following the impact. It can be deduced again from Fig. 14 that the effects of the inertia m_c and m_a are well decoupled for a low joint stiffness $k_s \leq 351$ Nm/rad.

Figure 15 represents the maximal impact force of the first impact obtained from the simulation of the two

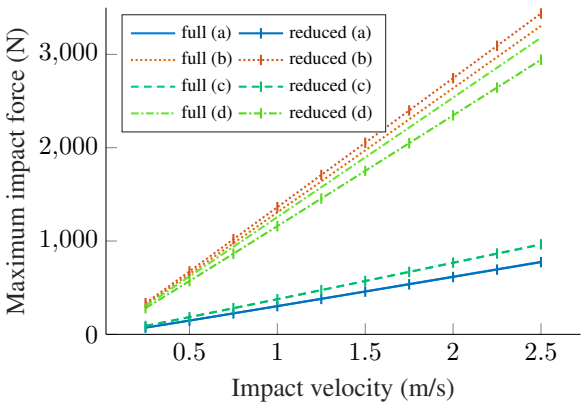

Fig. 9: Comparison of the maximum impact force obtained by simulation using the full model or the reduced mass-spring-mass model of the serial elastic RR robot, for the four impact scenarios with the head, considering a joint stiffness of 10^4 N.m/rad.

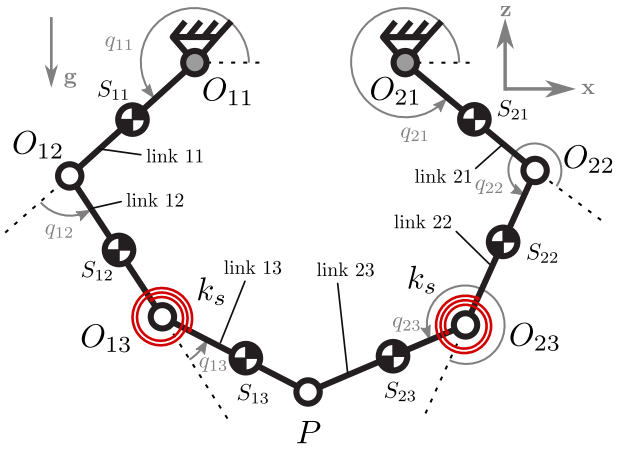

Fig. 10: Presentation of the R-Min robot, an underactuated seven-bar mechanism with rotational springs on distal joints O_{13} and O_{23}.

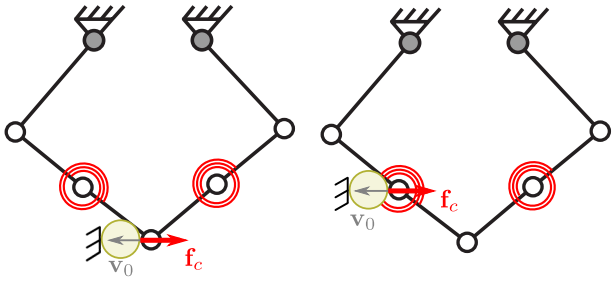

(a) Scenario (e): impact on the end effector

(b) Scenario (f): impact on the distal joint

Fig. 11: Description of the two simulated scenarios for the underactuated parallel R-Min robot.

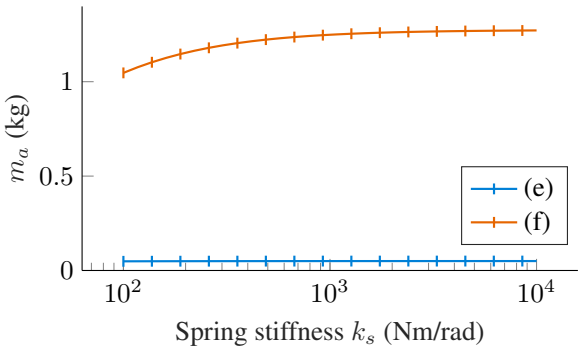

Fig. 12: Evolution of the reflected mass on the actuator side m_a with respect to the joint stiffness k_s for the two impact scenarios of the parallel R-Min robot: collision at the EE (scenario (e)), collision at the elbow O_{13} (scenario (f)).

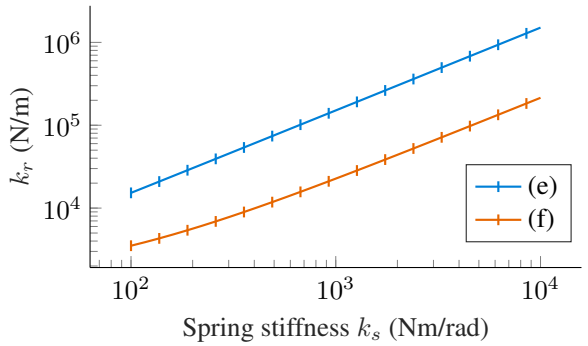

Fig. 13: Evolution of the reflected stiffness k_r with respect to the joint stiffness k_s for the two impact scenarios of the parallel R-Min robot: a contact at the EE (e), a contact at the elbow O_{13} (f).

scenarios (e) and (f), considering two different impacted body parts: the head and the chest. It can be deduced from this figure, that the reduced mass-spring-mass model allows to accurately approximate the maximal impact force, with a mean error of $\{3.6, 4.2\}$ % for an impact on the head and of $\{8.8, 13.8\}$ % for an impact on the chest for scenarios (e) and (f) respectively.

As a matter of comparison, simulations of a model considering a single mass m_c instead of the reduced mass-spring-mass system, provide a maximum impact force of $\{372, 222\}$ N resulting in an error of $\{4.6, 29.3\}$ % for an impact on the head and $\{160, 95\}$ N resulting in an error of $\{10.3, 51.2\}$ % for an impact on the chest (for scenarios $\{e, f\}$ respectively).

Discussion The variation of the maximal impact force with respect to the joint stiffness is quite dependent on the scenario. Indeed, the impact force is almost constant for scenario (e) (an impact at the EE), whereas it abruptly increases at a given joint stiffness for scenario (f) (an impact at the elbow O_{13}). For scenario (e), this can be explained by the fact that m_a is much lower than m_c, such that the inertia effect of m_a does not play any role in the resulting impact force. For scenario (f), the impact force suddenly increases when the joint stiffness exceeds a value such that the effects of inertia m_a and m_c are no longer decoupled. It can be seen from Fig. 15 that this transition stiffness can be well estimated using the reduced model.

It should be mentioned that the use of the reduced model allows to significantly reduce the duration of the simulation. Indeed, the simulation of an impact using the reduced model took an average time of 0.31 s versus 44.2 s with the full model. This makes the reduced model more practical for use in a process of optimization of the robot design when numerous simulations are necessary.

4 CONCLUSIONS

In this article, we introduced a method to compute the parameters of a reduced mass-spring-mass model of a compliant robot. This model allows to simulate, in a time-efficient manner, various impact scenarios: constrained or unconstrained cases, while considering the non-linear properties of the human body, and obtain the maximum impact force can in order to evaluate the hazard of a collision for a human being.

The reduced model is composed of two reflected masses and a stiffness in between. The two masses are obtained using a new set of generalized robot coordinates allowing to project the dynamics of the robot at the time of impact on two dynamically independent subspaces, a first subspace describing the dynamics at the contact location and a second subspace describing the remaining internal dynamics of the robot. The projection in this latter subspace is achieved using a newly introduced dynamically consistent generalized inverse. We then introduced a dynamically consistent reflected stiffness of the robot at the contact obtained from the Hessian of the potential energy computed at the time of impact, projected along the direction of impact using a dynamically consistent generalized inverse. Finally, the reflected mass on the actuator side is computed in such a way to minimize the error between a linearized model of a multi-link robot and its corresponding reduced mass-spring-mass model.

The precision of the proposed model was evaluated with respect to a corresponding full multi-link robot model for two case-studies, i.e. a two-dof elastic serial

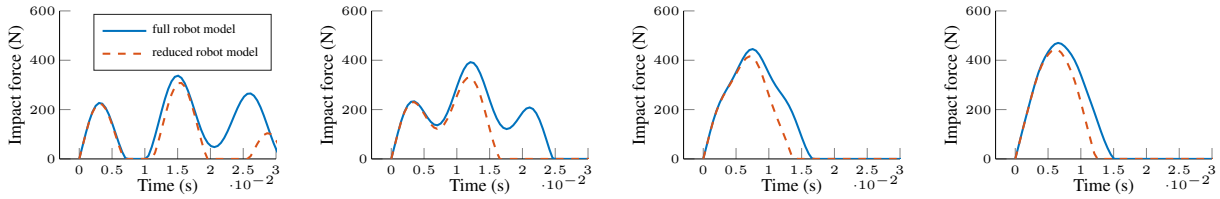

(a) $k_s = 100$ Nm/rad (b) $k_s = 351$ Nm/rad (c) $k_s = 1874$ Nm/rad (d) $k_s = 10000$ Nm/rad

Fig. 14: Comparison of the contact force time profiles obtained from the simulation of the full robot model (solid blue curves) and the reduced mass-spring-mass robot model (dashed red curves), for different values of the joint stiffness k_s, considering an impact at the elbow O_{13} (scenario (f)) between the R-Min robot and the head, with an impact velocity of 1 m/s.

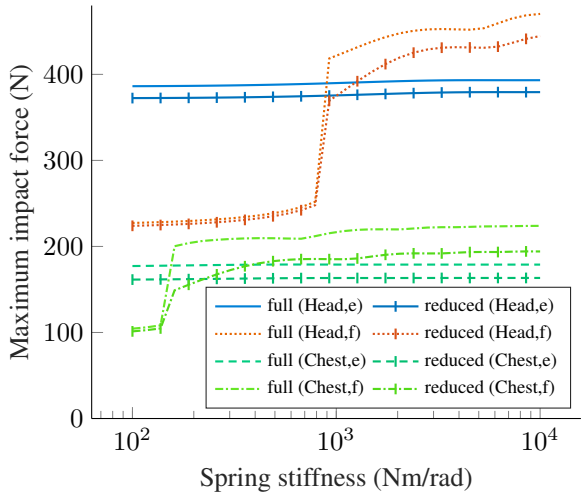

Fig. 15: Evolution of the maximum impact forces for an impact (a) at the elbow O_{13} and (b) at the EE. Two cases for the human are considered, a collision with the head and a collision with the chest.

robot and the R-Min robot, a seven-bar underactuated parallel robot. Simulation results show that the mass-spring-mass reduced model allows to precisely approximate the maximum impact force in various scenarios.

In future works, we will investigate using this reduced model in order to optimize the design parameters of a compliant robot, allowing to find the best trade-off between accuracy and safety.

APPENDIX A: LINEARIZATION OF THE DYNAMICS MODEL

Computation of the linearized model

Let us linearize the left-hand side of equation (2) around an equilibrium configuration $(\mathbf{q}_g = \mathbf{q}_{g0}, \dot{\mathbf{q}}_g = \mathbf{0}, \ddot{\mathbf{q}}_g = \mathbf{0})$. Let us call this function $\mathbf{h}$:

$$\mathbf{h}(\mathbf{q}_g, \dot{\mathbf{q}}_g, \ddot{\mathbf{q}}_g) = \mathbf{M}(\mathbf{q}_g)\ddot{\mathbf{q}}_g + \mathbf{g}(\mathbf{q}_g) + \mathbf{c}(\mathbf{q}_g, \dot{\mathbf{q}}_g) \quad (39)$$

Around an equilibrium configuration $(\mathbf{q}_g = \mathbf{q}_{g0}, \dot{\mathbf{q}}_g = \mathbf{0}, \ddot{\mathbf{q}}_g = \mathbf{0})$, we have:

$$\begin{aligned}\mathbf{h}(\mathbf{q}_g, \dot{\mathbf{q}}_g, \ddot{\mathbf{q}}_g) \approx \mathbf{h}(\mathbf{q}_{g0}, \mathbf{0}, \mathbf{0}) + \left.\frac{\partial \mathbf{h}}{\partial \ddot{\mathbf{q}}_g}\right|_{(\mathbf{q}_{g0},\mathbf{0},\mathbf{0})} \ddot{\mathbf{q}}_g \\ + \left.\frac{\partial \mathbf{h}}{\partial \dot{\mathbf{q}}_g}\right|_{(\mathbf{q}_{g0},\mathbf{0},\mathbf{0})} \dot{\mathbf{q}}_g + \left.\frac{\partial \mathbf{h}}{\partial \mathbf{q}_g}\right|_{(\mathbf{q}_{g0},\mathbf{0},\mathbf{0})} (\mathbf{q}_g - \mathbf{q}_{g0})\end{aligned} \quad (40)$$

A discussion on the reasons of choosing the linearization about the equilibrium configuration $(\mathbf{q}_g = \mathbf{q}_{g0}, \dot{\mathbf{q}}_g = \mathbf{0}, \ddot{\mathbf{q}}_g = \mathbf{0})$ and not another one with non-null accelerations and velocities is made at the end of App.A.

From the structure of Eq. (2), the different terms in (40) take the following forms:

$$\mathbf{h}(\mathbf{q}_{g0}, \mathbf{0}, \mathbf{0}) = \mathbf{g}(\mathbf{q}_{g0}) = \mathbf{g}_0 \quad (41)$$

$$\left.\frac{\partial \mathbf{h}}{\partial \ddot{\mathbf{q}}_g}\right|_{(\mathbf{q}_{g0},\mathbf{0},\mathbf{0})} = \mathbf{M}(\mathbf{q}_{g0}) = \mathbf{M}_0 \quad (42)$$

$$\left.\frac{\partial \mathbf{h}}{\partial \dot{\mathbf{q}}_g}\right|_{(\mathbf{q}_{g0},\mathbf{0},\mathbf{0})} = \mathbf{0} \quad (43)$$

$$\left.\frac{\partial \mathbf{h}}{\partial \mathbf{q}_g}\right|_{(\mathbf{q}_{g0},\mathbf{0},\mathbf{0})} = \frac{\partial \mathbf{g}(\mathbf{q}_{g0})}{\partial \mathbf{q}_g} = \frac{\partial^2 V(\mathbf{q}_{g0})}{\partial \mathbf{q}_g^2} \quad (44)$$

where $V(\mathbf{q}_{g0})$ is the robot potential energy[4] at $\mathbf{q}_{g0}$ and $\mathbf{M}_0$ is the inertia matrix at $\mathbf{q}_{g0}$. The term $\frac{\partial^2 V(\mathbf{q}_{g0})}{\partial \mathbf{q}_g^2}$ represent the stiffness matrix $\mathbf{K}_0$ of the robot:

$$\mathbf{K}_0 = \mathbf{K}(\mathbf{q}_{g0}) = \frac{\partial^2 V(\mathbf{q}_{g0})}{\partial \mathbf{q}_g^2} \tag{45}$$

It should be mentioned that, by definition, $\mathbf{K}_0$ is symmetric. As a result, introducing (40) and (44) into (2), the linearized dynamic model can be written under the form:

$$\mathbf{M}_0 \ddot{\mathbf{q}}_g + \mathbf{K}_0 \Delta \mathbf{q}_g = \Delta \mathbf{u} + \mathbf{f}_{ext} \tag{46}$$

where $\Delta \mathbf{q}_g = \mathbf{q}_g - \mathbf{q}_{g0}$ is a variation of the generalized coordinates and $\Delta \mathbf{u} = \mathbf{u} - \mathbf{g}_0$ is a variation of the generalized input forces around the equilibrium, and $\mathbf{f}_{ext}$ is the generalized contact force.

Discussion about the linearization of the robot dynamic model around the equilibrium configuration $(\mathbf{q}_g = \mathbf{q}_{g0}, \dot{\mathbf{q}}_g = \mathbf{0}, \ddot{\mathbf{q}}_g = \mathbf{0})$

In Section 2.2, we decided to linearize the dynamic model around the equilibrium configuration $(\mathbf{q}_g = \mathbf{q}_{g0}, \dot{\mathbf{q}}_g = \mathbf{0}, \ddot{\mathbf{q}}_g = \mathbf{0})$ while, during an impact, the velocity and the acceleration would be non null. We chose this equilibrium configuration because of the following considerations.

First, linearizing around a non null acceleration $\ddot{\mathbf{q}}_g = \ddot{\mathbf{q}}_{g0}$ would have only changed the expression of the matrix $\mathbf{K}_0$ that would have taken the following form:

$$\mathbf{K}_0 = \frac{\partial^2 V(\mathbf{q}_{g0})}{\partial \mathbf{q}_g^2} + \left.\frac{\partial (\mathbf{M}(\mathbf{q}_g)\ddot{\mathbf{q}}_{g0})}{\partial \mathbf{q}_g}\right|_{(\mathbf{q}_{g0})} \tag{47}$$

The term $\left.\frac{\partial (\mathbf{M}(\mathbf{q}_g)\ddot{\mathbf{q}}_g^*)}{\partial \mathbf{q}_g}\right|_{(\mathbf{q}_{g0})}$ is an additional dynamic stiffness. However, during the impact, the configuration $\mathbf{q}_g$ has a very small variation, and the derivative of the matrix $\mathbf{M}$ is very small. Thus, these terms can be neglected, as it is confirmed by the simulation of the considered case studies.

Then, linearizing around a non null velocity $\dot{\mathbf{q}}_g = \dot{\mathbf{q}}_{g0}$ would have changed two main things:

- The expression of the matrix $\mathbf{K}_0$ would have taken the following form:

$$\mathbf{K}_0 = \frac{\partial^2 V(\mathbf{q}_{g0})}{\partial \mathbf{q}_g^2} + \left.\frac{\partial \mathbf{c}(\mathbf{q}_g, \dot{\mathbf{q}}_g)}{\partial \mathbf{q}_g}\right|_{(\mathbf{q}_{g0}, \dot{\mathbf{q}}_{g0})} \tag{48}$$

  The variation of the Coriolis and Centrifugal effect with respect to the configuration is much smaller than their variation with respect to the velocity terms (vector $\mathbf{c}$ is quadratic in the velocity). Thus, as in the previous case, these terms can be neglected as it is confirmed by the simulation of the considered case studies.
- The term $\left.\frac{\partial \mathbf{h}}{\partial \dot{\mathbf{q}}_g}\right|_{(\mathbf{q}_{g0}, \mathbf{0}, \mathbf{0})}$ would have been different from zero, leading to a linear damping term in the equation (5). This damping term would have led to the obligation to add some damping in our simplified model (1), that was not necessary in our opinion, and as confirmed by the simulation of the considered case studies detailed in the next Section.

For all these reasons, we decided to linearize the model around the configuration $(\mathbf{q}_g = \mathbf{q}_{g0}, \dot{\mathbf{q}}_g = \mathbf{0}, \ddot{\mathbf{q}}_g = \mathbf{0})$. Obviously, the reduced model proposed in this work could be refined by using another equilibrium configuration.

APPENDIX B: A NEW SET OF GENERALIZED COORDINATES

In this Appendix, we want to verify that $\mathbf{q}_n = [x_c \ \mathbf{x}_a^T]^T$ is a new set of the robot generalized coordinates. Therefore, beginning from the definition of the generalised inverse matrices $\mathbf{J}_c^{\#}$ in Eq. (9) and $\mathbf{J}_a^{\#}$ in Eq. (15), we want to check that the jacobian matrices $\mathbf{J}_c$ and $\mathbf{J}_a$ satisfy the following properties (see Section 2.3):

$$\mathbf{J}_c \mathbf{J}_a^{\#} = \mathbf{0} \tag{49}$$

$$\mathbf{J}_a \mathbf{J}_a^{\#} = \mathbf{I}_{(n-1)\times(n-1)} \tag{50}$$

$$\mathbf{J}_a \mathbf{J}_c^{\#} = \mathbf{0} \tag{51}$$

$$\mathbf{J}_c \mathbf{J}_c^{\#} = 1 \tag{52}$$

with:

$$\mathbf{J}_c \dot{x}_c = \dot{\mathbf{q}}_g \tag{53}$$

$$\mathbf{J}_a \dot{\mathbf{x}}_a = \dot{\mathbf{q}}_g \tag{54}$$

$$\dot{\mathbf{q}}_g = \mathbf{J}_c^{\#} \dot{x}_c + \mathbf{J}_a^{\#} \dot{\mathbf{x}}_a \tag{55}$$

The properties (51) to (54) have been already proven in Section 2.3. Let us then focus, on the one hand, on the properties (49), (50), and, on the other hand, on (55).

[4]The stiffness due to a proportional controller can be added in the potential energy by using the expression $1/2(\mathbf{q}_a - \mathbf{q}_a^*)^T \mathbf{K}_p (\mathbf{q}_a - \mathbf{q}_a^*)$, where $\mathbf{K}_p$ is the matrix of proportional gains, $\mathbf{q}_a$ are the motor coordinates and $\mathbf{q}_a^*$ their reference configurations.

First, from the definitions (14) and (15) for $\mathbf{J}_a$ and $\mathbf{J}_a^{\#}$, it is possible to see, by left-multiplying (15) by $\mathbf{J}_c$, that we have:

$$\mathbf{J}_c\mathbf{J}_a^{\#} = \mathbf{J}_c\mathbf{M}_0^{-1}\mathbf{J}_a^T\mathbf{M}_a \tag{56}$$

Recalling that, by the definition (14), $\mathbf{J}_c\mathbf{M}_0^{-1}\mathbf{J}_a^T = \mathbf{0}$, we get

$$\mathbf{J}_c\mathbf{J}_a^{\#} = \mathbf{0} \tag{57}$$

which is the property (49). Moreover, from the definition of $\mathbf{M}_a$ in Eq. (16), we have

$$\mathbf{J}_a\mathbf{J}_a^{\#} = \mathbf{J}_a\mathbf{M}_0^{-1}\mathbf{J}_a^T\mathbf{M}_a = \mathbf{I}_{(n-1)\times(n-1)} \tag{58}$$

as should be obtained in (50).

Now, we need to prove that Eq. (55) is valid. For this, let us define a vector $\mathbf{z}$ such as:

$$\mathbf{z} = \mathbf{J}_c^{\#}\dot{x}_c + \mathbf{J}_a^{\#}\dot{\mathbf{x}}_a \tag{59}$$

Introducing (53) and (54) into (59), we have

$$\mathbf{z} = \left(\mathbf{J}_c^{\#}\mathbf{J}_c + \mathbf{J}_a^{\#}\mathbf{J}_a\right)\dot{\mathbf{q}}_g \tag{60}$$

Left-multiplying on one hand Eq. (60) by $\mathbf{J}_c$ and in the other hand by $\mathbf{J}_a$. We obtain the two following equations:

$$\mathbf{T}\mathbf{z} = \mathbf{T}\dot{\mathbf{q}}_g \tag{61}$$

where the matrix $\mathbf{T} \in \mathbb{R}^{n\times n}$ is square and defined by

$$\mathbf{T} = \begin{bmatrix}\mathbf{J}_c \\ \mathbf{J}_a\end{bmatrix} \tag{62}$$

$\mathbf{z} = \dot{\mathbf{q}}_g$ if and only if the square matrix $\mathbf{T}$ is of full rank. Because, by construction, $\mathbf{J}_a$ in (14) is full rank, and $\mathbf{J}_c$ in (4) is a single-row matrix, the condition for $\mathbf{T}$ to be full rank is that the rows of $\mathbf{J}_c$ and $\mathbf{J}_a$ are independent. To prove this, we can apply a Reductio ad absurdum. Let us assume that there exist a non null vector $\boldsymbol{\lambda_1}$ and a scalar λ_2 such that:

$$\boldsymbol{\lambda_1}\mathbf{J}_a + \lambda_2\mathbf{J}_c = \mathbf{0} \tag{63}$$

In other words, $\boldsymbol{\lambda_1}$ and λ_2 allows to show a linear dependency between the row of $\mathbf{J}_c$ and $\mathbf{J}_a$.

Let us right-multiply (63) by $\mathbf{J}_c^{\#}$. From the definition of $\mathbf{J}_a$ in (51), we have $\mathbf{J}_a\mathbf{J}_c^{\#} = \mathbf{0}$. Moreover, from (52), we have $\mathbf{J}_c\mathbf{J}_c^{\#} = 1$, which at the end, imposes $\lambda_2 = 0$. That is contrary to the initial assumption. The rows of the matrix $\mathbf{J}_c$ and $\mathbf{J}_a$ are thus independent. Moreover, $\mathbf{q}_n = [x_c\ \mathbf{x}_a^T]^T$ is a new set of generalized coordinates.

An interesting property If we take the eq. (60) and use the proven property that $\mathbf{w} = \dot{\mathbf{q}}_g$, then:

$$\mathbf{I}_{n\times n} = \mathbf{J}_c^{\#}\mathbf{J}_c + \mathbf{J}_a^{\#}\mathbf{J}_a \tag{64}$$

Using the definitions of $\mathbf{J}_c^{\#}$ and $\mathbf{J}_a^{\#}$ provided in (9) and (15), we get :

$$\mathbf{I}_{n\times n} = \mathbf{M}_0^{-1}\Big(\mathbf{J}_c^T\left(\mathbf{J}_c\mathbf{M}_0^{-1}\mathbf{J}_c^T\right)^{-1}\mathbf{J}_c + \mathbf{J}_a^T\left(\mathbf{J}_a\mathbf{M}_0^{-1}\mathbf{J}_a^T\right)^{-1}\mathbf{J}_a\Big) \tag{65}$$

Finally, left-multiplying by $\mathbf{M}_0$ and using (10) and (16),

$$\begin{aligned}\mathbf{M}_0 &= \mathbf{J}_c^T\left(\mathbf{J}_c\mathbf{M}_0^{-1}\mathbf{J}_c^T\right)^{-1}\mathbf{J}_c + \mathbf{J}_a^T\left(\mathbf{J}_a\mathbf{M}_0^{-1}\mathbf{J}_a^T\right)^{-1}\mathbf{J}_a \\ &= \mathbf{J}_c^T m_c\mathbf{J}_c + \mathbf{J}_a^T\mathbf{M}_a\mathbf{J}_a\end{aligned} \tag{66}$$

This expression shows that we have decoupled the inertia of our system in two subsystems. There is an inertia m_c at the level of the impact point C and a remaining inertia $\mathbf{M}_a$ in the rest of the robot.

REFERENCES

[1] Versace, J., 1971. "A review of the severity index". In Proc. 15th Stapp Car Crash Conf., SAE Technical Paper No. 710881, pp. 771–796.

[2] Haddadin, S., Albu-Schäffer, A., and Hirzinger, G., 2007. "Safety evaluation of physical human-robot interaction via crash-testing.". In Robotics: Science and systems, Vol. 3, Citeseer, pp. 217–224.

[3] Haddadin, S., Albu-Schäffer, A., and Hirzinger, G., 2008. "The role of the robot mass and velocity in physical human-robot interaction-part i: Non-constrained blunt impacts". In 2008 IEEE International Conference on Robotics and Automation, IEEE, pp. 1331–1338.

[4] ISO/TC 299 : ISO/TS15066, 2016. Robots and robotic devices – Collaborative robots. Tech. Rep. ISO/TS15066, International Organization for Standardization, Tech. Rep, february.

[5] Melia, M., Schmidt, M., Geissler, B., König, J., Krahn, U., Ottersbach, H. J., Letzel, S., and Muttray, A., 2015. "Measuring mechanical pain: the refinement and standardization of pressure pain threshold measurements". *Behavior research methods,* **47**(1), pp. 216–227.

[6] Haddadin, S., Albu-Schäffer, A., Frommberger, M., and Hirzinger, G., 2008. "The role of the robot mass and velocity in physical human-robot interaction-part ii: Constrained blunt impacts". In 2008 IEEE International Conference on Robotics and Automation, IEEE, pp. 1339–1345.

[7] Hirzinger, G., Sporer, N., Albu-Schäffer, A., Hahnle, M., Krenn, R., Pascucci, A., and Schedl, M., 2002. "Dlr's torque-controlled light weight robot iii-are we reaching the technological limits now?". In Proceedings 2002 IEEE International Conference on Robotics and Automation (Cat. No. 02CH37292), Vol. 2, IEEE, pp. 1710–1716.

[8] Kim, Y.-J., 2017. "Anthropomorphic low-inertia high-stiffness manipulator for high-speed safe interaction". *IEEE Transactions on robotics,* **33**(6), pp. 1358–1374.

[9] Bicchi, A., and Tonietti, G., 2004. "Fast and" soft-arm" tactics [robot arm design]". *IEEE Robotics & Automation Magazine,* **11**(2), pp. 22–33.

[10] Pratt, G. A., and Williamson, M. M., 1995. "Series elastic actuators". In Proceedings 1995 IEEE/RSJ International Conference on Intelligent Robots and Systems. Human Robot Interaction and Cooperative Robots, Vol. 1, IEEE, pp. 399–406.

[11] Pratt, J., Krupp, B., and Morse, C., 2002. "Series elastic actuators for high fidelity force control". *Industrial Robot: An International Journal*.

[12] Zinn, M., Roth, B., Khatib, O., and Salisbury, J. K., 2004. "A new actuation approach for human friendly robot design". *The international journal of robotics research,* **23**(4-5), pp. 379–398.

[13] Khatib, O., 1995. "Inertial Properties in Robotic Manipulation: An Object-Level Framework". *The International Journal of Robotics Research,* **14**(1), feb, pp. 19–36.

[14] Haddadin, S., Albu-Schäffer, A., Eiberger, O., and Hirzinger, G., 2010. "New insights concerning intrinsic joint elasticity for safety". In 2010 IEEE/RSJ International Conference on Intelligent Robots and Systems, IEEE, pp. 2181–2187.

[15] Kishi, Y., Yamada, Y., and Yokoyama, K., 2012. "The role of joint stiffness enhancing collision reaction performance of collaborative robot manipulators". In 2012 IEEE/RSJ International Conference on Intelligent Robots and Systems, IEEE, pp. 376–381.

[16] Lauzier, N., and Gosselin, C., 2015. "A comparison of the effectiveness of design approaches for human-friendly robots". *Journal of Mechanical Design,* **137**(8).

[17] Song, S., She, Y., Wang, J., and Su, H. J., 2020. "Toward Tradeoff between Impact Force Reduction and Maximum Safe Speed: Dynamic Parameter Optimization of Variable Stiffness Robots". *Journal of Mechanisms and Robotics,* **12**(5), pp. 1–8.

[18] Haddadin, S., Krieger, K., Mansfeld, N., and Albu-Schäffer, A., 2012. "On impact decoupling properties of elastic robots and time optimal velocity maximization on joint level". In 2012 IEEE/RSJ International Conference on Intelligent Robots and Systems, IEEE, pp. 5089–5096.

[19] Herbster, S., Behrens, R., and Elkmann, N., 2020. "A new approach to estimate the apparent mass of collaborative robot manipulators". In International Symposium on Experimental Robotics, Springer, pp. 211–221.

[20] She, Y., Song, S., Su, H.-J., and Wang, J., 2020. "A comparative study on the effect of mechanical compliance for a safe physical human–robot interaction". *Journal of Mechanical Design,* **142**(6).

[21] Seriani, S., Gallina, P., Scalera, L., and Lughi, V., 2018. "Development of n-dof preloaded structures for impact mitigation in cobots". *Journal of Mechanisms and Robotics,* **10**(5), p. 051009.

[22] Khalil, W., and Dombre, E., 2002. "Chapter 14 - motion control". In *Modeling, Identification and Control of Robots*, W. Khalil and E. Dombre, eds. Butterworth-Heinemann, Oxford, pp. 347–376.

[23] Khalil, W., and Dombre, E., 2004. *Modeling, Identification and Control of Robots*. Kogan Page Science paper edition Modeling, identification & control of robots. Elsevier Science.

[24] Albu-Schäffer, A., Fischer, M., Schreiber, G., Schoeppe, F., and Hirzinger, G., 2004. "Soft robotics: what cartesian stiffness can obtain with passively compliant, uncoupled joints?". In 2004 IEEE/RSJ International Conference on Intelligent Robots and Systems (IROS)(IEEE Cat. No. 04CH37566), Vol. 4, IEEE, pp. 3295–3301.

[25] Jeanneau, G., 2022. "Analyse et conception d'un robot parallèle sous-actionné intrinsèquement sûr". PhD thesis, École Centrale de Nantes.

[26] Jeanneau, G., Bégoc, V., and Briot, S., 2020.

"Geometrico-static analysis of a new collaborative parallel robot for safe physical interaction". In 2020 International Design Engineering Technical Conferences & Computers and Information in Engineering Conference (IDETC-CIE 2020).

[27] Jeanneau, G., Bégoc, V., Briot, S., and Goldsztejn, A., 2020. "R-Min: a fast collaborative underactuated parallel robot for pick-and-place operations". In 2020 IEEE International Conference on Robotics and Automation, IEEE.

[28] DGUV-Information, 2017. Collaborative robot systems design of systems with " power and force limiting " function. Available online at https://www.dguv.de/medien/fb-holzundmetall/publikationen-dokumente/infoblaetter/infobl_englisch/080_collaborativerobotsystems.pdf, updated on 08/2017.

[29] Vicentini, F., 2021. "Collaborative robotics: a survey". *Journal of Mechanical Design,* **143**(4), p. 040802.

[30] Jeanneau, G., Bégoc, V., and Briot, S., 2023. "Experimental safety analysis of r-min, an underactuated parallel robot". *Journal of Mechanisms and Robotics,* **15**(3), p. 031004.